

ORIGINAL ARTICLE

Multiscale design of high-voltage multilayer energy-storage ceramic capacitors

Ziming Cai¹  | Xiaohui Wang¹ | Bingcheng Luo¹ | Wei Hong^{2,3} | Longwen Wu¹ | Longtu Li¹

¹State Key Laboratory of New Ceramics and Fine Processing, School of Materials Science and Engineering, Tsinghua University, Beijing, China

²Department of Aerospace Engineering, Iowa State University, Ames, Iowa

³Global Station for Soft Matter, Global Institution for Collaborative Research and Education, Hokkaido University, Sapporo, Japan

Correspondence

Xiaohui Wang and Longtu Li, State Key Laboratory of New Ceramics and Fine Processing, School of Materials Science and Engineering, Tsinghua University, Beijing, China.

Emails: wxh@mail.tsinghua.edu.cn and llt-dms@mail.tsinghua.edu.cn

Funding information

This work was supported by Ministry of Sciences and Technology of China through National Basic Research Program of China (973 Program 2015CB654604); National Natural Science Foundation of China, Grant/Award Number: 51272123, 51672148; CBMI Construction Co., Ltd

Abstract

Multilayer energy-storage ceramic capacitors (MLESCCs) are studied by multiscale simulation methods. Electric field distribution of a selected area in a MLESCC is simulated at a macroscopic scale to analyze the effect of margin length on the breakdown strength of MLESCC using a finite element method. Phase field model is introduced to analyze the dielectric breakdown mechanism of MLESCC at a mesoscopic scale. The microstructure of selected area is generated through voronoi tessellation random construction routine containing core-shell-structured dielectric materials. The effects of margin length, shell permittivity, and shell volume fraction on the breakdown strength of MLESCC are respectively studied. Results indicate that the breakdown strength of MLESCC can be enhanced by adopting larger margin lengths, or by increasing the shell permittivity or volume fraction.

KEYWORDS

breakdown strength, core-shell, finite element method, MLESCC, multiscale design, phase field method

1 | INTRODUCTION

Dielectric capacitors are critical for advanced pulsed power systems due to their fast charging-discharging capability and high power density.¹⁻⁴ Recently, growing environmental problems and rapid development of renewable energy production demand a large amount of high energy density, environmental-friendly and low-cost energy-storage devices.⁵⁻⁷ Multilayer energy-storage ceramic capacitors (MLESCCs) possess very high volumetric capacitance and are suitable for chip surface mount with superior mechanical and thermal properties, which are promising candidates

for energy-storage device and other applications including hybrid electric vehicles and kinetic energy weapons.⁸⁻¹³ However, the low energy density and low working voltage limit these applications of MLESCCs. Theoretically, the energy density (J) of an MLESCC can be calculated by

$$J = \int_0^{D_{\max}} E dD, \quad (1)$$

where E , D and D_{\max} are, correspondingly, electric field strength, dielectric displacement, and the dielectric displacement under breakdown electric field. If we take dielectric permittivity ϵ as constant, the formula can be converted to

$$J = \frac{1}{2} \varepsilon E^2. \quad (2)$$

It is clear that the permittivity and breakdown strength are two major factors that determine the energy density of MLESCC.

MLESCCs are fabricated with hundreds of dielectric layers of small thicknesses arranged in parallel between metal internal electrodes.¹² The permittivity and breakdown strength are firstly determined. Through joint efforts of researchers in past decades, a great attention has been paid to prepare lead-free ceramics especially with core-shell-structured grains.^{6,7,14,15} Grain shells usually possess high breakdown strength and are more difficult to be damaged by the applied electric field than grain cores,^{16,17} which will enhance the breakdown strength of the entire ceramic and lead to high energy-storage density. Recently, a large recoverable energy-storage density of 4.03 J/cm³ with dielectric breakdown strength of 400 kV/cm was reported in 0.85KNN–0.15ST ceramics.¹⁸ Apart from the dielectric material properties, the design of internal electrode structure is also significant especially in high-voltage MLESCCs as the nonuniform distribution of local electric field induced by internal electrode structure will sharply reduce the breakdown voltage and thus drop the energy-storage density of MLESCCs.¹⁹ Yoon et al²⁰ successfully fabricated large size MLESCCs with reported capacitance of 0.46 μF/cm³ and dielectric loss of 0.65%, and the breakdown voltage reached 1450–1650 V depending on the array design of the internal electrodes.

During last few decades, the simulation and design of MLESCCs were mainly focused on the mechanical and thermal properties,^{21–24} but there was few work in modeling dielectric breakdown strength, which was the essential property of high-voltage MLESCCs. Wang et al¹⁹ calculated the concentration of local electric field although a two-dimensional finite element model by varying some geometric parameters of MLESCCs, and Malay et al²⁵ discussed the effect of microstructural defects on electric field distribution inside the MLESCC numerically. In this work, a multiscale simulation method is introduced to design

high-voltage MLESCCs based on dielectric breakdown behavior of MLESCC, which covers the geometric structure of MLESCC and the dielectric material with core-shell structure. First of all, the electric field distribution of a selected area in a MLESCC is calculated using a finite element method at a macroscopic scale to analyze the effect of margin length on the breakdown strength of MLESCC. After that, the phase field model based on mesoscopic is introduced to simulate the dielectric breakdown behavior of MLESCC. The microstructure of selected area is generated through voronoi tessellation random construction routine containing a core-shell-structured dielectric materials.^{26,27} Different margin length, shell permittivity, and shell fraction are, respectively, embedded into our phase field model to obtain a better design for high-voltage MLESCCs.

2 | MULTISCALE MODEL

For the breakdown simulation of an MLESCC, the schematic diagram of the MLESCC and the selected areas that are most likely to be damaged by applied electric field are shown in Figure 1. The thicknesses of dielectric layer and internal electrodes of the selected area are, respectively, 600 nm and 300 nm, typical for state-of-the-art MLESCCs.

The electric field distribution of this selected area is simulated at a macroscopic level using the finite element method through COMSOL Multiphysics 5.2a. The electric potential, ϕ , and electric field, $E = -\nabla\phi$, can be calculated by solving the Poisson's equation,²⁸ $\nabla(\varepsilon_0\varepsilon\nabla\phi) = 0$, where ε_0 is vacuum permittivity. The applied electric potential between the electrodes is set as 600 V, the permittivity of dielectric material (ε) is set as 1000, a typical value of barium titanate-(BT) based ceramic and the margin length varies from 2, 1.5, and 1 times the thickness of dielectric layer to analyze the effect of margin length on the breakdown strength of MLESCC. After that, a phase field model^{29,30} is introduced to simulate the dielectric breakdown process of MLESCC based on the mesoscopic geometric model. This model contains dielectric material

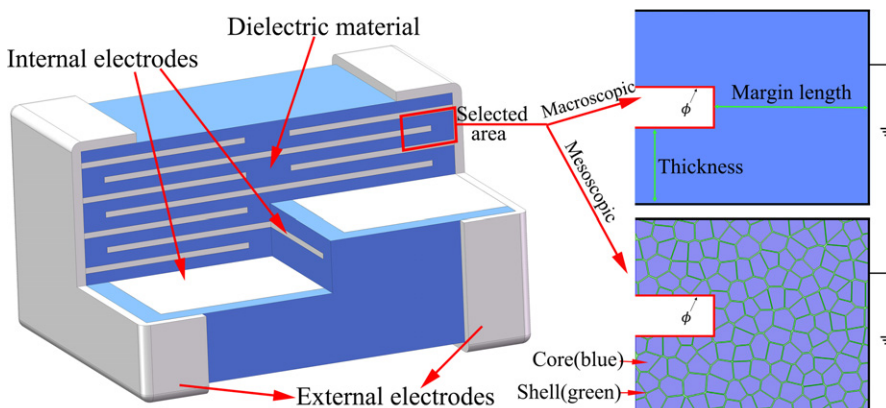


FIGURE 1 The schematic diagram and the selected typical area of MLESCC [Color figure can be viewed at wileyonlinelibrary.com]

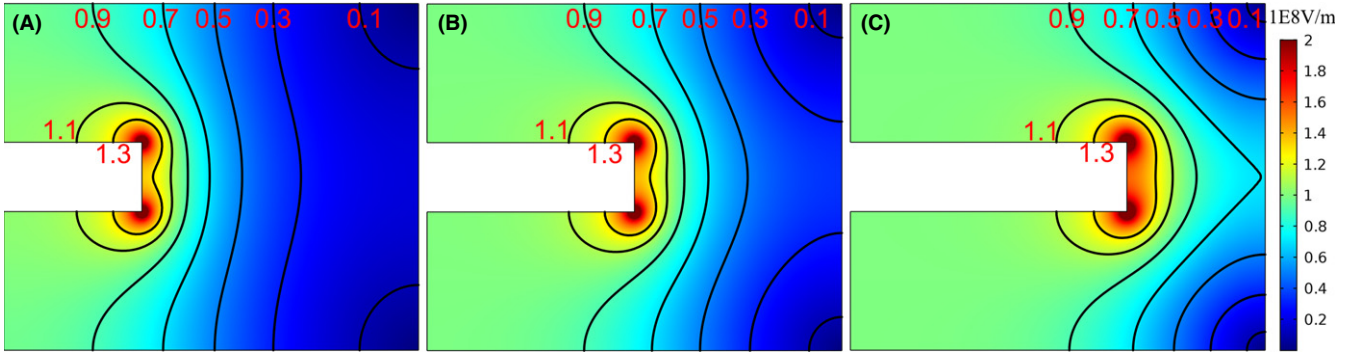


FIGURE 2 The electric field distribution of the selected area from MLESCC with the margin length being (A) 2, (B) 1.5 and (C) 1 times the thickness of dielectric layer and the contour lines are the equi-electric-field lines [Color figure can be viewed at wileyonlinelibrary.com]

with core-shell structure and the typical grain size used in the state-of-the-art MLESCC is 150 nm as seen in Figure 1. To characterize the breakdown process of a dielectric medium, we introduce a scalar phase field $s(x, y, t)$. The value of s varies from 1 to 0, which, respectively, represent the intact state and the fully damaged state. The fully damaged material becomes conductive, of which the permittivity is set as ϵ_{ini}/η , a large but finite number, where ϵ_{ini} is the initial permittivity and η is a small enough number, here, we take η as 1E-4 in our model. For any other intermediate state, the permittivity is interpolated by

$$\epsilon(s) = \frac{\epsilon_{ini}}{f(s) + \eta}, \quad (3)$$

where $f(s) = 4s^3 - 3s^4$. Furthermore, the dielectric material used in our model with core-shell structure is ferroelectric. The permittivity of grain core is electric field dependent, which can be described by Johnson's approximation³¹:

$$\epsilon_c(E) = \frac{\epsilon_c(0)}{(1 + kE^2)^{1/3}} \quad (4)$$

where, $\epsilon_c(0) = 1000$ is the zero-electric field permittivity typical for BT and $k = 3\beta(\epsilon_0\epsilon_c(0))^3$ is a constant that includes the nonlinear Johnson's parameter β . Meanwhile, the permittivity of grain shell (ϵ_s) is approximation linear. Thus, the permittivity of core-shell-structured ferroelectric material BT can be written as²⁸:

$$\epsilon_{ini}(E) = \begin{cases} \frac{\epsilon_c(0)}{(1 + kE^2)^{1/3}}, & \text{grain core} \\ \epsilon_s, & \text{grain shell} \end{cases} \quad (5)$$

In this model, the energy of system consists of complementary electrostatic energy per unit volume,

$$W_{es}(E, s) = \begin{cases} -\int_0^{E_{max}} \frac{\epsilon_c(s)E}{(1+kE^2)^{1/3}} dE, & \text{grain core} \\ -\frac{\epsilon_s(s)}{2} E \cdot E, & \text{grain shell} \end{cases},$$

breakdown energy, $W_d(s) = W_c[1 - f(s)]$, and gradient energy term to regulate sharp phase boundaries, with W_c

representing the critical density of electrostatic energy. The material parameter Γ is approximately the breakdown energy. Breakdown occurs if such process decreases the total potential energy of the system

$$\Pi[s, \phi] = \int_{\Omega} [W_{es}(E, s) + W_d(s) + W_i(\nabla s)] dV. \quad (6)$$

According to linear kinetic law: $\partial s / \partial t = -m \delta \Pi / \delta s$, with mobility m as a material parameter that features the speed of breakdown propagation in nanocomposites, the eventually normalized governing equations of dimensionless form can be written as:

$$\begin{cases} \nabla \cdot [\bar{\epsilon}_c(s)(1 + k\nabla\bar{\phi} \cdot \nabla\bar{\phi})^{-1/3} \nabla\bar{\phi}] = 0, & \text{grain core} \\ \nabla \cdot [\bar{\epsilon}_s(s) \nabla\bar{\phi}] = 0, & \text{grain shell} \end{cases} \quad (7)$$

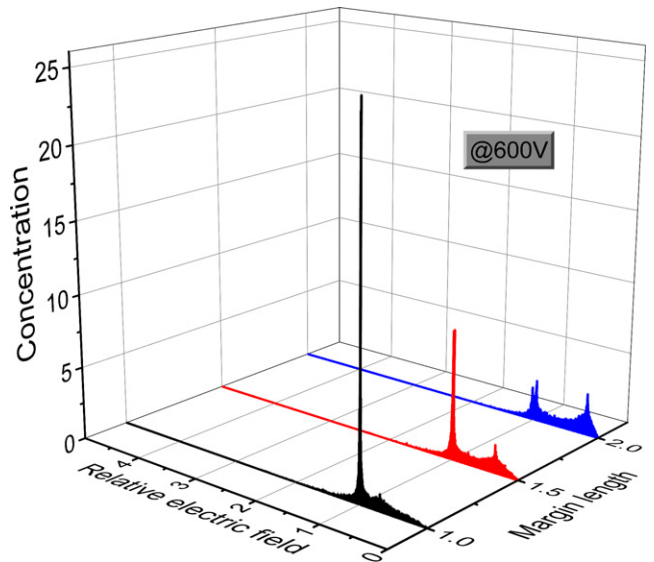


FIGURE 3 Probability distribution of electric field named concentration counted by statistically summarizing the relative electric field strength to the applied electric field inside the selected area at various margin length [Color figure can be viewed at wileyonlinelibrary.com]

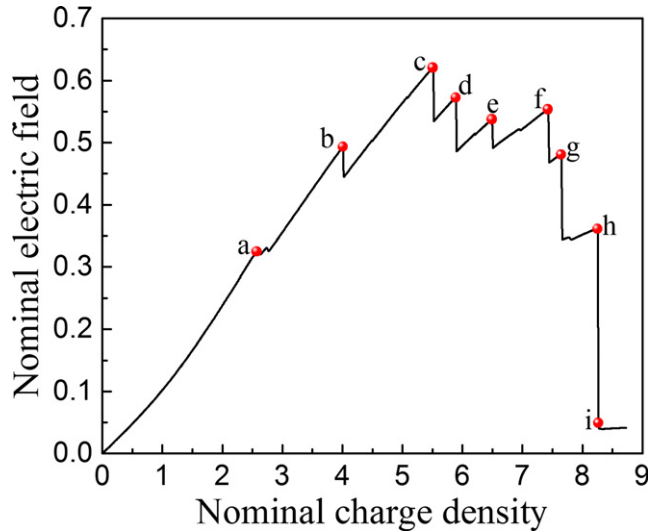


FIGURE 4 The nominal field-charge-density relation of selected area in MLESCC with the margin length as two times the thickness dielectric layer, and the shell permittivity and volume fraction 100% and 10% [Color figure can be viewed at wileyonlinelibrary.com]

$$\begin{cases} \frac{\partial s}{\partial t} = -\frac{3\bar{\epsilon}'_c(s)}{4k} ((1 + \bar{k}\bar{\nabla}\bar{\phi} \cdot \bar{\nabla}\bar{\phi})^{2/3} - 1) + f'(s) \\ \quad + \frac{1}{2}\bar{\nabla}^2 s, & \text{grain core} \\ \frac{\partial s}{\partial t} = \frac{\bar{\epsilon}'_s(s)}{2}\bar{\nabla}\bar{\phi} \cdot \bar{\nabla}\bar{\phi} + f'(s) + \frac{1}{2}\bar{\nabla}^2 s, & \text{grain shell} \end{cases} \quad (8)$$

in which the corresponding quantities are symbolised with over-bars. Generally, the permittivity of grain core is considered higher than that of grain shell, while the breakdown energy is about the same. The breakdown energy is set as $\Gamma_c/\Gamma_s = 1/10$, the nonlinear factor is taken as $k = 5E4 \text{ m}^2 \cdot \text{V}^{-2}$, and the permittivity of grain shell in our model varies among 5, 10, and 100, approximately, the permittivity of SiO_2 ,²⁶ Al_2O_3 ,³² TiO_2 ,²⁸ respectively. Thus, $\epsilon_c(0)/\epsilon_s$ separately equals 200, 100, and 10. This phase field model is calculated by implementing the equations (7) and (8) into COMSOL Multiphysics 5.2a. Limited by the computational power, all simulations are carried out in two-dimensional (2D) domains.

3 | RESULTS AND DISCUSSION

3.1 | Margin length design of MLESCC through macroscopic model (finite element model)

The tips of internal electrodes are the place where the distribution of electric field is most nonuniformity. Therefore, a 2D domain containing an internal electrode tip is selected as seen in Figure 1. The electric field distribution of the selected area from MLESCC with the margin length being

2, 1.5, and 1 times the thickness of dielectric layer is shown in Figure 2. We can figure out that the electric field strength near the tip of internal electrode (dark red area) is several times larger than that in uniform domain (green area). Meanwhile, along the increase in margin length, the concentrated area of electric field where the electric field strength is larger than the uniform strength reduces to some extent. Such improvement of electric field distribution will enhance the breakdown voltage of MLESCCs. To get a more precise distribution of electric field, the probability distribution of electric field which comes from mesh points named concentration is counted by statistically summarizing the relative electric field strength to the applied electric field through MATLAB as seen in Figure 3. It is clear that as the margin length reducing, the concentration peak of relative electric field moves to higher level with the concentration counts enhanced several times, which indicates that the breakdown probability of MLESCC with small margin length is higher than that with large margin length according to the theory of Weibull distribution.³³ Thus, a larger margin length design of MLESCC is necessary.

3.2 | Margin length, shell permittivity, and volume fraction design of MLESCC through mesoscopic model (phase field model)

A closer look at the dielectric breakdown process inside the selected area of MLESCC is simulated using a phase field model with the core-shell-structured dielectric material BT, generated through voronoi tessellation random construction routine through MATLAB by given random seed points. The margin length of the model is set as two times the thickness of dielectric layer, and the shell permittivity and volume fraction 100% and 10%. The dielectric breakdown process can be described by the nominal field-charge-density relation as shown in Figure 4. The field-charge-density curve below dot “a” shows the nonlinear dielectric, typical behavior of ferroelectric ceramic. Simultaneously, the snapshots of the breakdown process and the electric field distribution during breakdown of the selected area are, respectively, shown in Figures 5 and 6. Combine Figures 4 and 5, it can be summarized that as the nominal charge density increases, the nominal electric field rises as well. The MLESCC keeps undamaged until the nominal charge density reaches dot “a” in Figure 4 and the dielectric breakdown starts at the tip of internal electrode, where the local electric field concentrates most as seen in Figure 5A. Then, it will propagate through the grain core. However, when the breakdown path reaches grain shell, the field-charge-density curve will wind as the breakdown energy of shell is larger than core, which means the shell is harder to be damaged, yet the higher permittivity of shell makes it share a higher electric field. Therefore, the

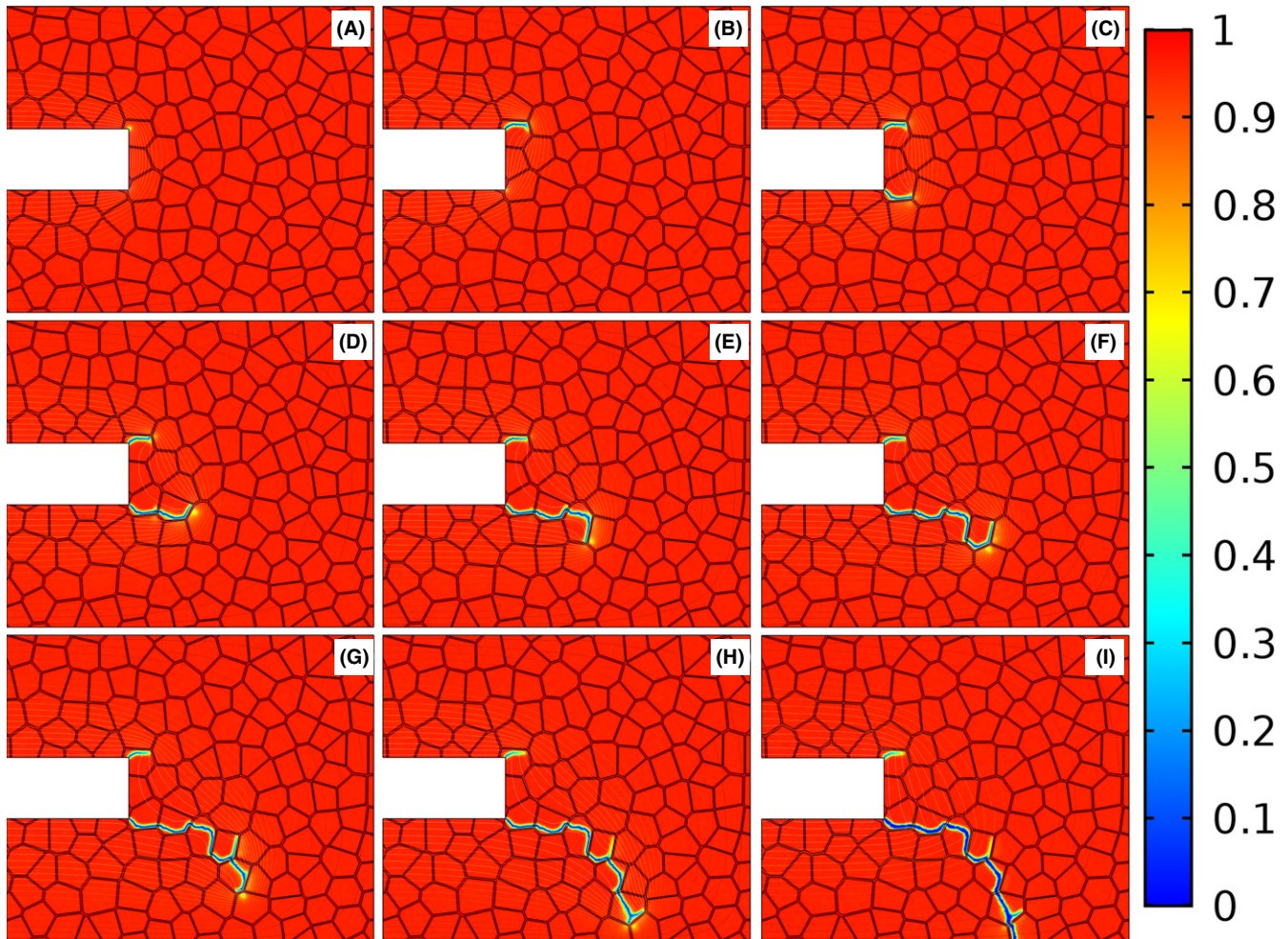


FIGURE 5 (A-I) Snapshots of the breakdown process of selected area in MLESCC. (A-I) correspond to the dots A-I in Figure 4 [Color figure can be viewed at wileyonlinelibrary.com]

nominal electric field slightly reduces. After passing through the grain shell, the nominal electric field continues to ascend. The electric field strength in the forefront of the breakdown path is always the most concentrated domain as seen in Figure 6. Until the breakdown path passes through all grain and reaches the negative electrode, the nominal electric field suddenly falls to zero, which indicates that the MLESCC is fully damaged and becomes a conductive (internal electric field strength is zero) as shown in Figures 5I and 6I. The highest nominal electric field through the entire breakdown process is taken as the nominal breakdown strength of MLESCC.

To compare the results in Section 3.1, three different geometric models are established with the same margin length setting in macroscopic model, respectively, 2, 1.5, and 1 times the thickness of dielectric layer, with the average grain size of 150 nm and the shell permittivity and volume fraction of 100% and 10% separately. The breakdown path images of the selected area in MLESCC and the nominal field-charge-density relation at various margin length are shown in Figure 7. We can easily figure out that the

larger the margin length, the higher the breakdown strength of MLESCC, which is in great consistent with the results of our macroscopic models. Upon closer analysis, the breakdown path reaches the right external electrode when the margin length is same as the thickness of dielectric layer; however, as the margin length increases, the breakdown path eventually reaches the internal negative electrode and need to pass across more grains, which will also enhance the breakdown strength.

Other critical material parameters can be changed by the fabrication process are the shell permittivity and volume fraction. Consequently, the shell permittivity and volume fraction are also changed in our phase field models to compare the dielectric breakdown strength of MLESCCs with different cases. Firstly, the permittivity of grain shell in our model varies 5, 10, and 100, approximately the permittivity of SiO_2 , Al_2O_3 , TiO_2 , with the margin length and shell volume fraction remaining 2 times the thickness of dielectric layer and 10% as seen in Figure 8. The breakdown path images of the selected area in MLESCC and the nominal field-charge-density relation at various shell permittivity are

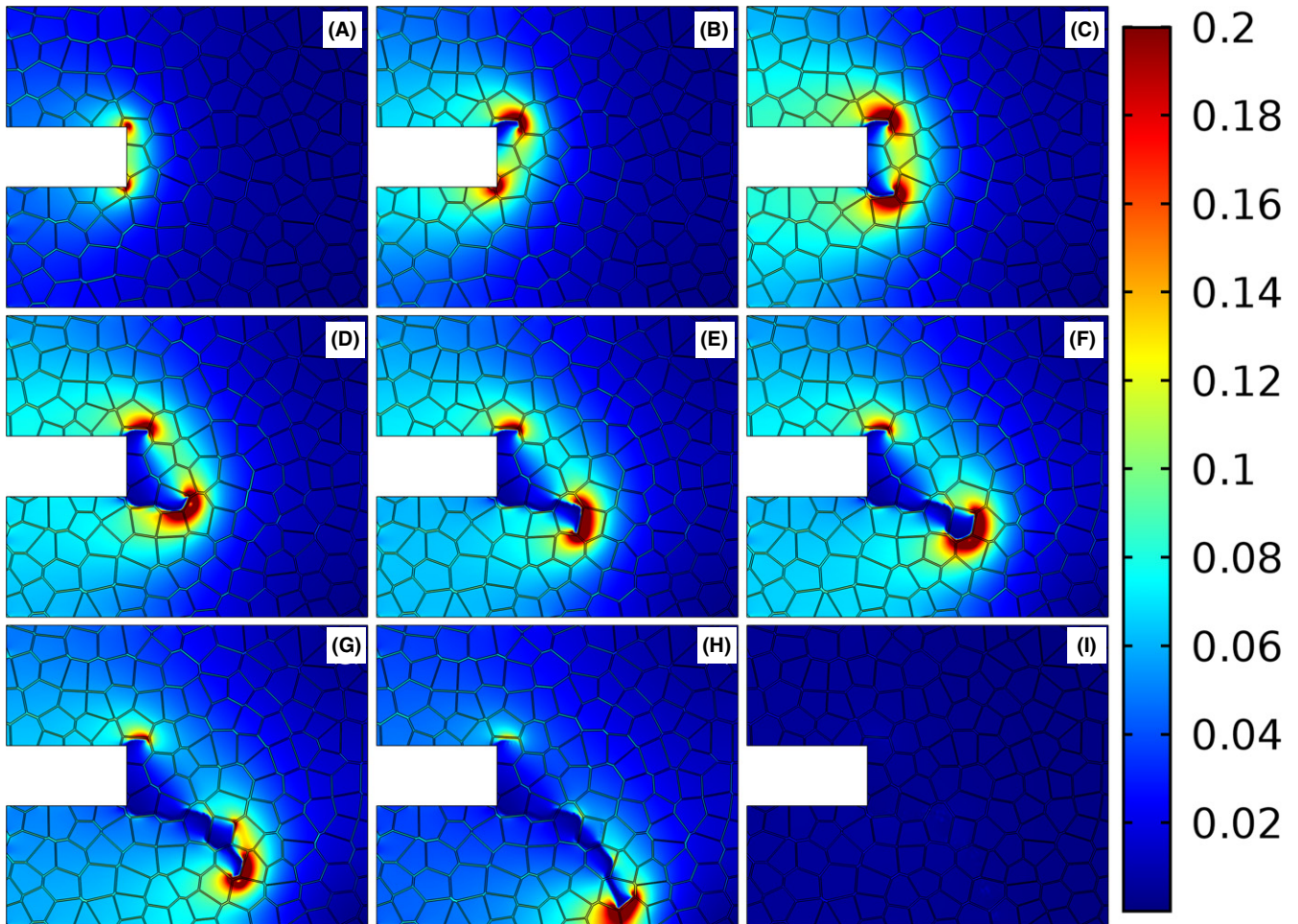


FIGURE 6 (A-I) Snapshots of the electric field distribution during breakdown process of selected area in MLESCC. (A-I) correspond to the dots A-I in Figure 4 [Color figure can be viewed at [wileyonlinelibrary.com](#)]

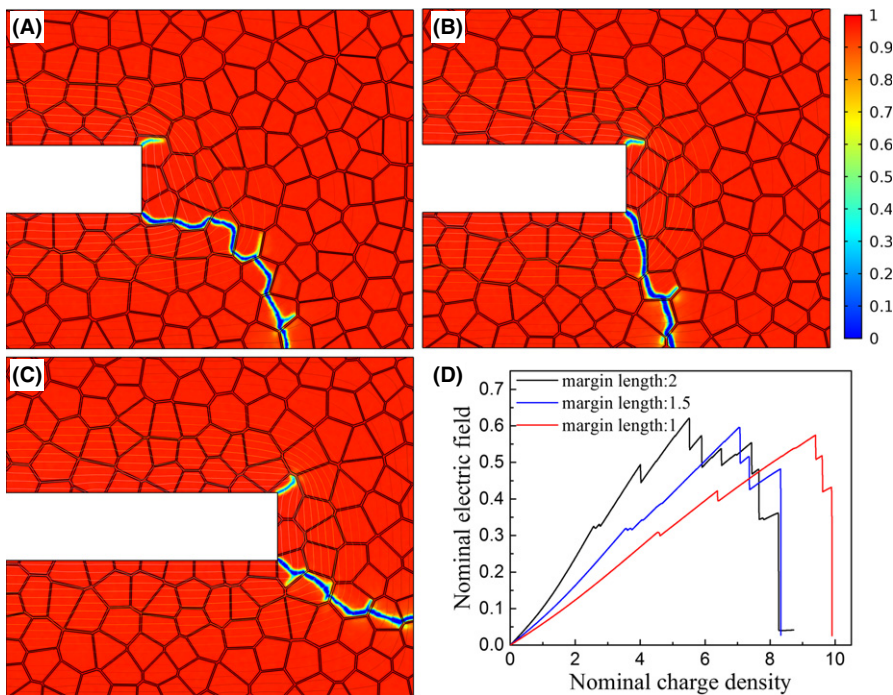


FIGURE 7 The breakdown path images of selected area in MLESCC with the margin length: (A) 2, (B) 1.5 and (C) 1 times the dielectric material thickness marked as 2, 1.5, and 1 in (D). (D) The nominal field-charge-density relation of all these three types corresponding to (A), (B), and (C) [Color figure can be viewed at [wileyonlinelibrary.com](#)]

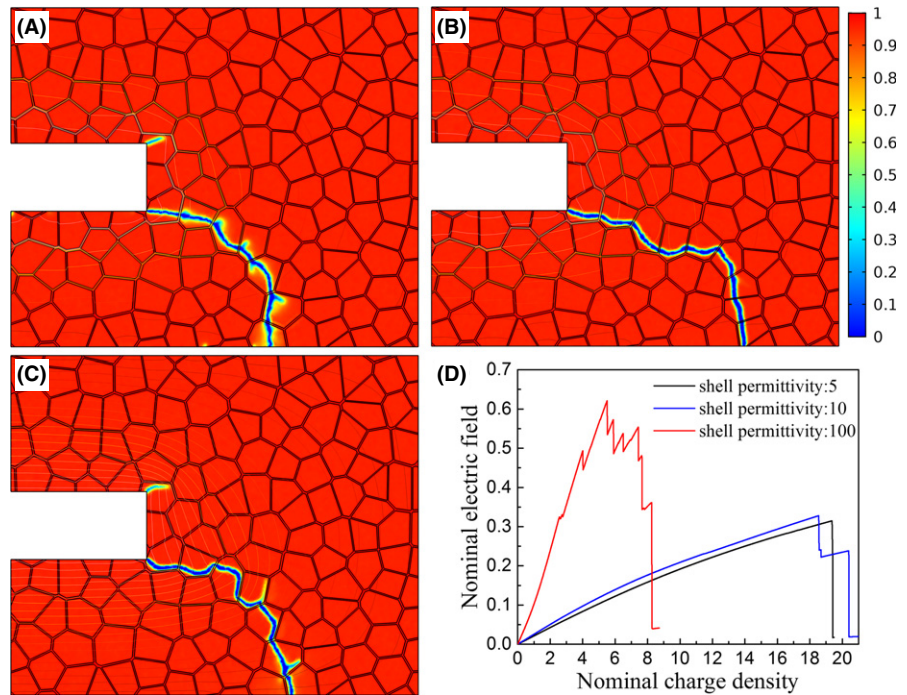


FIGURE 8 The breakdown path images of selected area in MLESCC with the shell permittivity: (A) 100, (B) 10 and (C) 5. (D) The nominal field-charge-density relation of all these three types corresponding to (A), (B), and (C) [Color figure can be viewed at wileyonlinelibrary.com]

shown in Figure 8. It is clear that the breakdown strength of MLESCC with shell permittivity of 100 is almost three times higher than that with shell permittivity of 10 and 5. The huge permittivity difference in grain core and shell will lead to enormous electric field strength between them. The smaller shell permittivity comes smaller electric field strength in grain core. Thus, to obtain the same nominal electric field, the selected area with low permittivity needs larger nominal charge density. That is why the slope of field-charge-density curve with shell permittivity of 5 and

10 is far smaller than that of 100. Therefore, when prepare the dielectric material with core-shell structure, a higher shell permittivity will be a better choice. Next, the phase field models with the grain shell fraction varying 5%, 10%, and 15% are established, of which the margin length and shell permittivity keep 2 times the thickness of dielectric layer and 100 unchanged. The breakdown path images of the selected area in MLESCC and the nominal field-charge-density relation at various shell fraction are shown in Figure 9. It is found that as the shell fraction grows, the

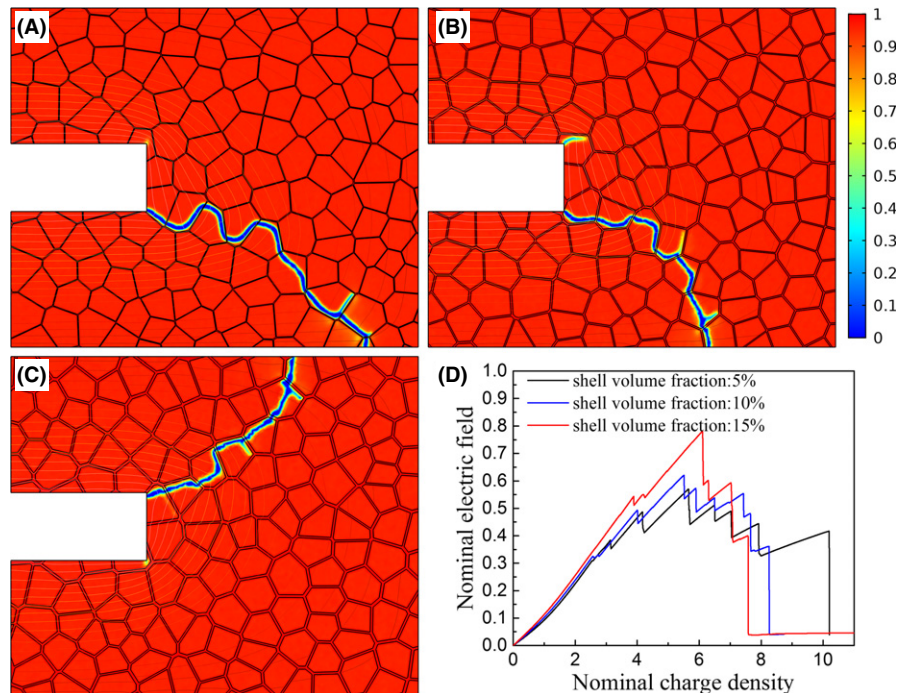


FIGURE 9 The breakdown path images of selected area in MLESCC with the shell fraction: (A) 5%, (B) 10%, and (C) 15%. (D) The nominal field-charge-density relation of all these three types corresponding to (A-C) [Color figure can be viewed at wileyonlinelibrary.com]

breakdown strength of MLESCC is enlarged as well. This is easy to understand that the breakdown energy of grain shell is higher than grain core. Thus, the breakdown path propagates inside the selected region of MLESCC will be blocked by the grain shell and the more volume fraction of grain shell, such blocking effect will be more obvious, which results in a higher breakdown strength of MLESCC.

4 | CONCLUSION

A multiscale simulation method containing macroscopic and mesoscopic models is introduced to design MLESCCs. The key geometric parameter, margin length of MLESCCs, is studied both two models and the results are well consistent with each other. It is suggested that the larger margin length will enhance the dielectric breakdown strength of MLESCCs. Moreover, the crucial material properties parameters, namely the permittivity and volume fraction of grain shell, are carefully discussed in our mesoscopic phase field model with core-shell-structured dielectric material. Results indicate that a larger shell permittivity close to the grain core will improve the nonuniformity distribution of electric field and thus elevate the breakdown strength of MLESCCs. Larger shell volume fraction comes higher breakdown strength, as the grain shell is more difficult to breakdown compared with grain core. All conclusion above not only gives a deeper understanding of dielectric breakdown mechanism but also provides a better suggestion for design high-voltage MLESCCs.

ACKNOWLEDGMENT

The work was supported by Ministry of Sciences and Technology of China through National Basic Research Program of China (973 Program 2015CB654604), National Natural Science Foundation of China (Grant No. 51272123, 51672148), and also supported by CBMI Construction Co., Ltd. In addition, our work is completed on the “Explorer 100” cluster system of Tsinghua National Laboratory for Information Science and Technology.

ORCID

Ziming Cai  <http://orcid.org/0000-0001-8026-023X>

REFERENCES

1. Qu B, Du H, Yang Z, et al. Large recoverable energy storage density and low sintering temperature in potassium-sodium niobate-based ceramics for multilayer pulsed power capacitors. *J Am Ceram Soc.* 2017;100:1516-1526.
2. Dang ZM, Zheng MS, Zha JW. 1D/2D carbon nanomaterial-polymer dielectric composites with high permittivity for power energy storage applications. *Small.* 2016;12:1688-1701.
3. Li Q, Han K, Gadinski MR, et al. High energy and power density capacitors from solution-processed ternary ferroelectric polymer nanocomposites. *Adv Mater.* 2014;26:6244-6249.
4. Dang ZM, Yuan JK, Yao SH, et al. Flexible nanodielectric materials with high permittivity for power energy storage. *Adv Mater.* 2013;25:6334-6365.
5. Hao Y, Wang X, Bi K, et al. Significantly enhanced energy storage performance promoted by ultimate sized ferroelectric BaTiO₃ fillers in nanocomposite films. *Nano Energy.* 2017;31:49-56.
6. Wu L, Wang X, Gong H, et al. Core-satellite BaTiO₃@SrTiO₃ assemblies for a local compositionally graded relaxor ferroelectric capacitor with enhanced energy storage density and high energy efficiency. *J Mater Chem C.* 2015;3:750-758.
7. Hao X. A review on the dielectric materials for high energy-storage application. *J Adv Dielectr.* 2013;03:1330001.
8. Kumar N, Ionin A, Ansell T, et al. Multilayer ceramic capacitors based on relaxor BaTiO₃-Bi(Zn_{1/2}Ti_{1/2})O₃ for temperature stable and high energy density capacitor applications. *Appl Phys Lett.* 2015;106:549.
9. Love GR. Energy storage in ceramic dielectrics. *J Am Ceram Soc.* 1990;73:323-328.
10. Groh C, Kobayashi K, Shimizu H, et al. High-temperature multilayer ceramic capacitors based on 100-x(94Bi_{1/2}Na_{1/2}TiO₃-6BaTiO₃)-xK_{0.5}Na_{0.5}NbO₃. *J Am Ceram Soc.* 2016;99:2040-2046.
11. Bultitude J, Jones L, Xu B, et al. An evaluation of BME COG multilayer ceramic capacitors as building blocks for DC-Link capacitors in 3-D power electronics. *International Symposium on 3d Power Electronics Integration and Manufacturing. IEEE.* 2016.
12. Pan M-J, Randall CA. A brief introduction to ceramic capacitors. *IEEE T Dielect El In.* 2010;26:44-50.
13. Xu X, Gurav AS, Lessner PM, et al. Robust bme class-i mlccs for harsh-environment applications. *IEEE Trans Industr Electron.* 2011;58:2636-2643.
14. Wu L, Wang X, Li L. Core-shell BaTiO₃@SrTiO₃ particles for local graded dielectric ceramics with enhanced temperature stability and energy storage capability. *J Alloy Compd.* 2016;688:113-121.
15. Aman S, Kubo K, Akiba H, et al. Core-shell structure and dielectric properties of (K_{0.5}Na_{0.5})NbO₃-SrZrO₃ for high-temperature capacitors. *Jpn J Appl Phys.* 2016;55:10 TB08.
16. Song Z, Liu H, Hao H, et al. Effect of the grain boundary on the dielectric breakdown strength of (Ba_{0.4}Sr_{0.6})TiO₃ paraelectric ceramics with various grain sizes. 2014 Joint IEEE International Symposium on the Applications of Ferroelectrics, International Workshop on Acoustic Transduction Materials and Devices & Workshop on Piezoresponse Force Microscopy (Isaf/Iwatmd/Pfm). 2014;204-207.
17. Touzin M, Goeriot D, Fitting HJ, et al. Relationships between dielectric breakdown resistance and charge transport in alumina materials—effects of the microstructure. *J Eur Ceram Soc.* 2007;27:1193-1197.
18. Yang Z, Du H, Qu S, et al. Significantly enhanced energy storage density in transparent potassium-sodium niobate-based lead free ceramics. *J Mater Chem A.* 2016;4:13778-13785.

19. Wang Y, Li L, Ma Z, et al. The inner electrode structure and its optimization for high voltage chip capacitors. *J Funct Mater (Chinese)*. 2003;34:414-417.
20. Yoon J-R, Moon BH, Lee HY, et al. Design and analysis of electrical properties of a multilayer ceramic capacitor module for DC-link of hybrid electric vehicles. *J Electr Eng Technol*. 2013;8:808-812.
21. Huang C-W, Chen B-T, Chen K-Y, et al. Finite element analysis and design of thermal-mechanical stresses in multilayer ceramic capacitors. *Int J Appl Ceram Technol*. 2015;12:451-460.
22. Chen K-Y, Huang C-W, Wu M, et al. Control of stress concentration in surface-mounted multilayer ceramic capacitor subjected to bending. *J Am Ceram Soc*. 2014;97:1170-1176.
23. Jiang W-G, Feng X-Q, Nan C-W. Influence of residual thermal stresses and geometric parameters on stress and electric fields in multilayer ceramic capacitors under electric bias. *J Phys D Appl Phys*. 2008;41:135310.
24. Franken K, Maier HR, Prume K, et al. Finite-element analysis of ceramic multilayer capacitors: failure probability caused by wave soldering and bending loads. *J Am Ceram Soc*. 2000;83:1433-1440.
25. Samantaray MM, Gurav A, Dickey EC, et al. Electrode defects in multilayer capacitors part ii: finite element analysis of local field enhancement and leakage current in three-dimensional microstructures. *J Am Ceram Soc*. 2012;95:264-268.
26. Wu L, Wang X, Li L, et al. Enhanced energy density in core-shell ferroelectric ceramics: modeling and practical conclusions. *J Am Ceram Soc*. 2016;99:930-937.
27. Dean J, Foeller P, Reaney I, et al. A resource efficient design strategy to optimise the temperature coefficient of capacitance of BaTiO₃-based ceramics using finite element modelling. *J Mater Chem A*. 2016;4:6896-6901.
28. Lin S, Lu T, Jin C, et al. Size effect on the dielectric properties of BaTiO₃ nanoceramics in a modified ginsburg-landau-devonshire thermodynamic theory. *Phys Rev B*. 2006;74:134115.
29. Hong W, Pitike KC. Modeling Breakdown-resistant Composite Dielectrics. *Procedia Iutam*. 2015;12:73-82.
30. Pitike KC, Hong W. Phase-field model for dielectric breakdown in solids. *J Appl Phys*. 2014;115:8.
31. Johnson KM. Variation of dielectric constant with voltage in ferroelectrics and its application to parametric devices. *J Appl Phys*. 1962;33:2826-2831.
32. Liu B, Wang X, Zhao Q, et al. Improved energy storage properties of fine-crystalline BaTiO₃ ceramics by coating powders with Al₂O₃ and SiO₂. *J Am Ceram Soc*. 2015;98:2641-2646.
33. Weibull W. A statistical distribution function of wide applicability. *J Appl Mech-Trans ASME*. 1951;18:293-297.

How to cite this article: Cai Z, Wang X, Luo B, Hong W, Wu L, Li L. Multiscale design of high-voltage multilayer energy-storage ceramic capacitors. *J Am Ceram Soc*. 2018;101:1607-1615.
<https://doi.org/10.1111/jace.15322>